



## Centennial- to millennial-scale hard rock erosion rates deduced from luminescence-depth profiles

Sohbati, Reza; Liu, Jinfeng; Jain, Mayank; Murray, Andrew ; Egholm, David; Paris, Richard; Guralnik, Benny

*Published in:*  
Earth and Planetary Science Letters

*Link to article, DOI:*  
[10.1016/j.epsl.2018.04.017](https://doi.org/10.1016/j.epsl.2018.04.017)

*Publication date:*  
2018

*Document Version*  
Peer reviewed version

[Link back to DTU Orbit](#)

*Citation (APA):*  
Sohbati, R., Liu, J., Jain, M., Murray, A., Egholm, D., Paris, R., & Guralnik, B. (2018). Centennial- to millennial-scale hard rock erosion rates deduced from luminescence-depth profiles. *Earth and Planetary Science Letters*, 493, 218-230. <https://doi.org/10.1016/j.epsl.2018.04.017>

---

### General rights

Copyright and moral rights for the publications made accessible in the public portal are retained by the authors and/or other copyright owners and it is a condition of accessing publications that users recognise and abide by the legal requirements associated with these rights.

- Users may download and print one copy of any publication from the public portal for the purpose of private study or research.
- You may not further distribute the material or use it for any profit-making activity or commercial gain
- You may freely distribute the URL identifying the publication in the public portal

If you believe that this document breaches copyright please contact us providing details, and we will remove access to the work immediately and investigate your claim.

# Centennial- to millennial-scale hard rock erosion rates deduced from luminescence-depth profiles

Reza Sohbati<sup>a,b</sup>, Jinfeng Liu<sup>c,\*</sup>, Mayank Jain<sup>a</sup>, Andrew Murray<sup>b</sup>, David Egholm<sup>d</sup>, Richard Paris<sup>e</sup>,  
Benny Guralnik<sup>b,f</sup>

<sup>a</sup>Center for Nuclear Technologies, Technical University of Denmark, DK 4000 Roskilde, Denmark

<sup>b</sup>The Nordic Laboratory for Luminescence Dating, Department of Geoscience, Aarhus University, DK 4000 Roskilde,  
Denmark

<sup>c</sup>State Key Laboratory of Earthquake Dynamics, Institute of Geology, China Earthquake Administration, China

<sup>d</sup>Department of Geoscience, Aarhus University, 8000 Aarhus, Denmark

<sup>e</sup>Department of Computing and Mathematics, University of Abertay, Dundee DD1 1HG, UK

<sup>f</sup>Soil Geography and Landscape group and the Netherlands Centre for Luminescence Dating, Wageningen University,  
Droevendaalsesteeg 3, 6708PB Wageningen, The Netherlands

\*Corresponding author: [liujf81@ies.ac.cn](mailto:liujf81@ies.ac.cn)

## Abstract

The measurement of erosion and weathering rates in different geomorphic settings and over diverse temporal and spatial scales is fundamental to the quantification of rates and patterns of earth surface processes. A knowledge of the rates of these surface processes helps one to decipher their relative contribution to landscape evolution – information that is crucial to understanding the interaction between climate, tectonics and landscape. Consequently, a wide range of techniques has been

23 developed to determine short- ( $<10^2$  a) and long-term ( $> 10^4$  a) erosion rates. However, no method is  
24 available to quantify hard rock erosion rates at centennial to millennial timescales. Here we propose a  
25 novel technique, based on the solar bleaching of luminescence signals with depth into rock surfaces, to  
26 bridge this analytical gap. We apply our technique to glacial and landslide boulders in the Eastern  
27 Pamirs, China. The calculated erosion rates from the smooth varnished surfaces of 7 out of the 8  
28 boulders sampled in this study vary between  $< 0.038 \pm 0.002$  and  $1.72 \pm 0.04$  mm ka<sup>-1</sup> (the eighth boulder  
29 gave an anomalously high erosion rate, possibly due to a recent chipping/cracking loss of surface).  
30 Given this preferential sampling of smooth surfaces, assumed to arise from grain-by-grain surface loss,  
31 we consider these rates as minimum estimates of rock surface denudation rates in the Eastern Pamirs,  
32 China.

## 33 **1. Introduction**

34 The erosion of the Earth's surface results from a combination of physical, chemical and biological  
35 weathering and the subsequent removal of weathering products by various transport agents. Erosion of  
36 rock surfaces may result from a range of processes such as dissolution, grain-by-grain attrition,  
37 chipping/frost cracking, and even massive bedrock landslides. Quantifying the rates and timing of such  
38 processes over various spatial and temporal scales is fundamental to determining the relative  
39 contribution of each process and thereby understanding landscape evolution. Bare hard rock surfaces  
40 are the most durable surficial features in the landscape and thus can have a long memory of the  
41 erosional history. Consequently, a wide range of methods have been developed to quantify erosion  
42 rates of subaerially-exposed rock surfaces (Turkowski and Cook, 2017). These include: i) the  
43 direct/indirect measurement of surface loss over laboratory timescales, or by comparison with resistant  
44 natural or anthropogenic reference features of known-age (Stephenson and Finlayson, 2009; Moses et

45 al., 2014), ii) the analysis of cosmogenic nuclides (CNs) produced within mineral grains from exposed  
46 rock surfaces as a result of bombardment by secondary cosmic rays (Nishizumi et al., 1986; Lal, 1991),  
47 and iii) thermochronology using a wide range of radiogenic processes to determine the thermal history  
48 of rocks, and thus their exhumation rates (Braun et al., 2006). Depending on the length of the  
49 observation period or the age of the reference feature, the rates measured by the techniques in category  
50 (i) are integrated over sub-annual to multi-decadal timescales (Moses et al., 2014), while the rates  
51 derived using CNs and thermochronology are averaged over thousands to millions of years,  
52 respectively (Lal, 1991, Braun et al., 2006). The short (i.e.  $< 10^2$  years) and long (i.e.  $> 10^4$  years)  
53 timescales of these techniques leave an intermediate time interval of  $10^2$ – $10^4$  years over which there is  
54 currently no technique available for quantifying the erosion rates of rock surfaces. The centennial to  
55 millennial time intervals are of particular importance and interest to human society for evaluating the  
56 effects of climate change or anthropogenic activity on landscape evolution.

57 One of the major challenges in geomorphology is to make a link between different scales of  
58 observation (Schumm and Litchy, 1965; Warke and McKinley, 2011). Specifically, the timescale over  
59 which the rates of earth surface processes are averaged directly influences the apparent rates (e.g.  
60 Gardner et al., 1987; Viles, 2001; Koppes and Montgomery, 2009). Such measurement-interval bias  
61 can result in either underestimation (e.g. Kirchner et al., 2001) or overestimation (e.g. Lal et al., 2005)  
62 of short-term measurements compared to long-term average rates, hindering a linkage by simple  
63 extrapolation between the rates averaged over timescales that are orders of magnitude different  
64 (Gardner et al., 1987). It is clear that the development of a new analytical tool to bridge the gap  
65 between the decadal and millennial timescales would be of considerable value in erosion studies.

66 Several studies have shown that when a rock surface is first exposed to daylight, the latent  
67 luminescence, mainly from the constituent minerals quartz and feldspar, starts to decrease. The rate

68 of this resetting (or ‘bleaching’) process decreases with depth as the incident light is attenuated (e.g.  
69 Habermann et al., 2000; Laskaris and Liritzis, 2011). Based on this phenomenon, Sohbati et al. (2011,  
70 2012a,b) proposed a new surface-exposure dating technique, which utilizes the time and depth  
71 dependence of the residual latent luminescence. The longer the rock is exposed to daylight, the deeper  
72 is the transition zone between the region of bleached latent luminescence at the surface and saturated  
73 latent luminescence at depth. After calibration, the depth of this “optical bleaching front” can be  
74 translated to an exposure time (Sohbati et al., 2011, 2012a,b).

75 CN-depth profiles are influenced by the effect of erosion; Lal (1991) points out that the rock depth  
76 equivalent to one absorption mean free path for cosmic rays is ~50 cm. In contrast, the corresponding  
77 absorption mean free path for light penetration into rocks is on the scale of millimetres (Sohbati et al.,  
78 2011, 2012a,b). Thus, luminescence-depth profiles are expected to be ~2 orders of magnitude more  
79 sensitive to the effect of erosion. In contrast to the effect of daylight exposure, the transition zone  
80 between the surface bleached latent luminescence and the saturated latent luminescence will become  
81 shallower, the higher the erosion rate. Nevertheless, this effect has been considered to be unimportant  
82 in all published applications, because the technique was applied to surfaces where archaeological  
83 evidence suggested negligible erosion (e.g. Pederson et al., 2014). However, the application of the  
84 technique to geological features, where constraints on surface preservation are rare on the centimetre  
85 scale (Lehmann et al., 2018 being an exception), necessitates the effect of erosion be taken into account  
86 (Sanderson et al., 2011). Here, we present a further development of the luminescence surface-exposure  
87 dating model (Sohbati et al., 2012b) that includes the effect of erosion on luminescence-depth profiles.  
88 We then use the new model to derive steady-state centennial- to millennial-scale hard-rock erosion  
89 rates from several surface-exposed glacial and landslide boulders from the Pamir plateau, China.

90           **2. Theoretical framework**

91           The ubiquitous rock-forming minerals quartz and feldspar can store energy (in the form of trapped  
92 charge) through the absorption of ionizing radiation resulting from the decay of naturally-occurring  
93 radionuclides (mainly  $^{238}\text{U}$  and  $^{232}\text{Th}$  and their decay products, and  $^{40}\text{K}$ ) and cosmic rays. This trapped  
94 charge can be released during exposure to heat or light. Some of the energy released during the  
95 resetting is emitted as photons (i.e. as UV, visible, or near infrared luminescence); if the trapped charge  
96 is released by light (i.e. photon stimulation of trapped electrons), the luminescence emitted from the  
97 mineral is called optically stimulated luminescence (OSL; Aitken, 1998). OSL is now a well-  
98 established Quaternary dating method usually used to determine the time elapsed since mineral grains  
99 were last exposed to daylight (i.e. the burial age) (Aitken, 1998). Recently, luminescence has also been  
100 shown to be useful in surface exposure dating (Sohbati et al., 2012a, b).

101           **2.1. Luminescence surface exposure age**

102           In any rock sample that has been deeply buried and therefore shielded from light for an extended  
103 length of time (typically  $> 0.5$  Ma) the trapped electron population in the constituent quartz and  
104 feldspar crystals will usually be in field saturation due to finite trapping capacity (e.g. Guralnik et al.,  
105 2013). If the rock is then exposed to daylight by an exhumation event (e.g. fracture, ice-scouring) the  
106 trapped electron population will begin to decrease. The electron detrapping rate decreases with depth as  
107 a result of the attenuation of incident light with depth, following Beer-Lambert law (e.g. Laskaris and  
108 Liritzis, 2011). The rate of change of trapped electron population at a particular depth is a result of  
109 competition between two effects: (i) the accumulation rate of trapped electrons due to ambient ionizing  
110 radiation, and (ii) the eviction rate of trapped electrons due to the daylight flux at a given depth. Thus,  
111 in a rock that has been exposed to daylight, the residual luminescence forms a sigmoidal profile that

112 continues to evolve with time until it reaches secular equilibrium, when electron trapping and  
 113 detrapping rates are equal at all depths (Fig. 1a). For a given exposure time and daylight conditions, the  
 114 penetration depth and form of a luminescence profile depend on the opacity of the rock-forming  
 115 minerals and the relevant photoionization cross section(s). Assuming that luminescence signal is  
 116 proportional to the trapped electron population, Sohbaty et al. (2011, 2012a, b) developed a  
 117 mathematical model describing the luminescence-depth profiles in rock surfaces and demonstrated its  
 118 application in surface exposure dating. According to this model, which assumes first-order kinetics for  
 119 electron trapping and detrapping, the instantaneous concentration of trapped electrons  $n$  ( $\text{mm}^{-3}$ ) at a  
 120 depth of  $x$  (mm) can be expressed as:

$$\frac{dn}{dt} = (N - n)F(x) - nE(x) \quad (1)$$

121 where  $t$  (ka) is time,  $N$  ( $\text{mm}^{-3}$ ) is the concentration of electron traps, and  $F(x)$  and  $E(x)$  (both  $\text{ka}^{-1}$ ) are  
 122 the rate constants describing electron trap filling and emptying, respectively.

123  $E(x)$  ( $\text{ka}^{-1}$ ) decreases with depth due to attenuation of daylight intensity into the rock following the  
 124 Beer-Lambert law:

$$E(x) = \overline{\sigma\varphi_0} e^{-\mu x} \quad (2)$$

125 where  $\overline{\sigma\varphi_0}$  ( $\text{ka}^{-1}$ ) is the time-averaged detrapping rate constant at the surface of the rock and  $\mu$  ( $\text{mm}^{-1}$ )  
 126 is the inverse of the mean free path of photons in the rock.

127 The coefficient  $F(x)$  describes the trapping rate constant:

$$F(x) = \dot{D}(x) / D_0 \quad (3)$$

129 where  $\dot{D}$  ( $\text{Gy ka}^{-1}$ ) is the natural dose rate and  $D_0$  (Gy) is the characteristic dose that fills ~63% (i.e.  
 130  $1 - e^{-1}$ ) of the traps (Wintle and Murray, 2006).  $D_0$  is an intrinsic property of the dosimeter and not  
 131 expected to have any systematic dependence on depth.  $\dot{D}$  may have a weak dependence on depth into

132 the rock, especially close to the surface (e.g. Sohbati et al., 2015) due to short range of the beta  
133 particles, but this can be neglected for exposure dating, since near the surface,  $E(x)$  exceeds  $F(x)$  by  
134 many orders of magnitude. Thus, in the present context, the dose rate may well be approximated as a  
135 depth-independent constant, i.e.  $F(x) \approx F = \text{const}$ .

136 When a previously shielded rock is first exposed to light, the initial trapped electron population  
137  $n_0 \cong N$ , assuming a stable trapped electron population. Solving Eqn. (1) with the boundary condition  
138 of  $n = N$  at  $t = 0$  yields:

$$\frac{n(x, t)}{N} = \frac{E(x)e^{-t[E(x)+F]} + F}{E(x) + F} \quad (4)$$

139 According to this model, as the exposure time increases, the luminescence profile advances further  
140 into the rock until  $dn/dt \cong 0$  at all depths (Fig. 1a). In the absence of erosion (i.e. with a time-  
141 invariant  $x$ ), the model can be used to derive exposure ages as old as 100 ka, depending on the values  
142 of the model parameters (Sohbati et al., 2012a, b) (Fig. 1a).

143 The millimetre depth scale of the luminescence resetting profiles, however, make them highly  
144 susceptible to the effect of erosion (i.e.  $x$  decreases with time). In any case, the assumption of zero  
145 erosion is far from true for most terrestrial surfaces (e.g. Portenga and Bierman, 2011). Any exfoliation  
146 of the rock surface and/or removal of bleached material from the surface due to weathering and erosion  
147 moves the luminescence profile closer to the surface, preventing the derivation of a simple exposure  
148 age. Below, we explore the effect of erosion on luminescence-depth profiles with the aim of deriving  
149 erosion rates from such data.

150 **2.2. Luminescence steady-state erosion rate**

151 The spatially-uniform removal of the uppermost material from a column of rock at a steady rate  $\varepsilon$   
 152 (mm ka<sup>-1</sup>), affects the depth of all underlying material as follows:

$$\frac{dx}{dt} = -\varepsilon \quad (5)$$

153 where  $\varepsilon \geq 0$ . Eqn. (5) can be integrated with regard to time to yield  $x(t) = x_0 - \varepsilon t$ , where  $x_0$  is an  
 154 arbitrary depth datum. Substitution of a time-dependent depth  $x(t)$  from Eqn. (5) into the electron  
 155 detrapping rate constant  $E(x)$  (Eqn. 2) results in:

$$E(x(t)) = \overline{\sigma\varphi_0} e^{-\mu(x_0 - \varepsilon t)} = (\overline{\sigma\varphi_0} e^{-\mu x_0}) e^{\mu\varepsilon t} = E_0 e^{\mu\varepsilon t} \quad (6)$$

156 where  $E_0 = \overline{\sigma\varphi_0} e^{-\mu x_0}$  is the trap emptying rate constant at  $x_0$ . The substitution of Eqn. (6) into Eqn.  
 157 (1) yields:

$$\frac{dn}{dt} = (N - n)F - nE_0 e^{\mu\varepsilon t} \quad (7)$$

158 which is functionally identical to the description of a luminescence-thermochronometer (Guralnik et  
 159 al., 2013), except for the sign within the exponential. This subtle difference, i.e. the trap emptying rate  
 160 increases (rather than diminishes) with time, leads to a substantially different solution for  $n$  (Appendix  
 161 A). To describe steady-state erosion, we define the datum depth to be infinitely deep (i.e.  $x_0 = \infty$ ) (Lal,  
 162 1991), and obtain an analytical solution for Eqn. (7):

$$\frac{n(x, \varepsilon)}{N} = M\left(1, 1 + \frac{F}{\mu\varepsilon}, -\frac{E(x)}{\mu\varepsilon}\right) \quad (8)$$

163 where  $M$  is the confluent hypergeometric function (Abramowitz and Stegun, 1964), readily available in  
 164 the majority of common computing software (Appendix A). Eqn. (8) describes the luminescence-depth  
 165 profile in a rock surface that has been continuously eroding at a rate  $\varepsilon$  (mm ka<sup>-1</sup>) (Fig. 1b).

166 A luminescence-depth profile can be interpreted either in terms of an apparent exposure age (Eqn.  
167 4) or an apparent steady-state erosion rate (Eqn. 8). As in CN dating, in the absence of other  
168 information one cannot choose between the two interpretations (Lal, 1991); an independent constraint  
169 on age or erosion rate is required to identify which model to select and so derive the true erosion rate or  
170 age, respectively. Provided that all other model parameters (i.e.  $\dot{D}$ ,  $D_0$ ,  $\mu$ , and  $\overline{\sigma\phi_0}$ ) are quantified, the  
171 exposure age ( $t$ ) or erosion rate ( $\varepsilon$ ) can be derived from an observed luminescence-depth profile via  
172 fitting of Eqns. (4) or (8), respectively.

173 In practice, there is a limit to how well a profile can be distinguished from a profile in secular  
174 equilibrium. Any luminescence-depth profile can be characterized by the depth  $x_{50\%}$ , at which the  
175 signal intensity drops to 50% of that in saturation (at depth). In a steady-state profile, this depth  $x_{50\%,SS}$   
176 can be easily predicted from Eq. (4) (when  $t \rightarrow \infty$ ). Here, we make a conservative assumption that a  
177 depth difference of at least one mean free path (i.e.  $1/\mu$ ) is required to experimentally distinguish a  
178 transient profile from a predicted steady-state profile. This means the apparent exposure age or erosion  
179 rate of any profile whose ( $x_{50\%} > x_{50\%,SS} - 1/\mu$ ) should be considered as apparent minimum age or  
180 maximum erosion rate, respectively.

181 We now test both the luminescence surface exposure and erosion rate models by applying them to  
182 several glacial and landslide boulders in the Eastern Pamirs, China. The surface exposure ages of all  
183 these boulders have been previously established using  $^{10}\text{Be}$  dating.

### 184 **3. Study area and sampling sites**

185 The Tashkurgan Valley stretches NNW for ~100 km along the trace of the Karakoram and  
186 Tashkurgan faults, marking the junction between the Karakoram, Pamir and Western Tibet (Fig. 2).  
187 The valley floor contains many landslide and glacial erratic boulders whose chronology can provide

188 valuable information about the driving mechanisms such as enhanced earthquake activity and climate  
189 change (Owen et al., 2012; Yuan et al., 2013). As a result, the area has been subject to extensive  
190 research in recent years, mostly based on CN surface exposure dating of boulders. Tens of glacial and  
191 landslide boulders have been dated using  $^{10}\text{Be}$  by various workers (e.g. Seong et al., 2009a,b,c; Owen  
192 et al., 2012; Yuan et al., 2013; Xu and Yi, 2014), providing an excellent independent-age control  
193 dataset for our model verification.

194 At different locations along the valley, we visited three sites previously studied by others (Seong et  
195 al., 2009a; Owen et al., 2012; Yuan et al., 2013) (Fig. 2). These locations were selected based on (i)  
196 well-constrained chronology as shown by converging  $^{10}\text{Be}$  ages obtained from several ( $> 6$ ) boulders at  
197 each site, and (ii) ages covering a wide range of 7 to 70 ka (Fig. 2). We sampled the flat tops of large  
198 boulders ( $> 2$  m in diameter) close to the points previously sampled for CN dating, as well as the  
199 exposed surfaces of a few smaller boulders ( $< 1$  m in diameter) close to the large boulders (Fig. 3).  
200 These were most likely deposited at the same time as the large boulders, but they are usually dismissed  
201 in CN studies, mainly because of concerns related to post-depositional reworking. Boulder surfaces  
202 varied from being smooth, visually homogenous with various degrees of desert varnish to more  
203 sporadic cm-scale exfoliation (Figs. 3 and 4). Sub-mm- to mm-scale weathering and grain loss was  
204 evidenced by friable surfaces from which individual grains could be readily removed by light  
205 mechanical abrasion (rubbing by hand). Samples were collected from surfaces with abundant desert  
206 varnish, where we assume chipping is probably a less important surface removal mechanism.

## 207 **4. Methods**

### 208 **4.1. Sampling and sample preparation**

209 Blocks of  $\sim 4 \times 4 \times 7 \text{ cm}^3$  were cut from the boulder surfaces using a petrol-driven cut-off saw  
210 equipped with a dry-cut diamond blade (Fig. 3). Blocks were immediately wrapped in aluminium foil  
211 and light-tight plastic bags to avoid any further exposure to daylight after collection. Under subdued  
212 red-orange light in the laboratory, cores 10 mm in diameter and up to 50 mm long were drilled into  
213 blocks using a water-cooled diamond core drill; these cores were then cut into 1.2 mm thick slices  
214 using a water-cooled low-speed saw equipped with a 0.3 mm thick diamond wafer blade, giving a net  
215 slice spacing of 1.5 mm. The outermost slices were treated by 10% HF for 40 min. and 10% HCl for 20  
216 min. to remove any weathering products. No treatment was given to inner slices (Sohbati et al., 2011).

217 A subsample of  $\sim 150 \text{ g}$  was also prepared from each sample for dose rate measurement. These were  
218 pulverized, homogenized and then cast in wax to prevent radon loss and to provide a reproducible  
219 counting geometry. They were then stored for at least three weeks to allow  $^{222}\text{Rn}$  to reach equilibrium  
220 with its parent  $^{226}\text{Ra}$  before the measurement.

### 221 **4.2. Analytical facilities and measurements**

222 Although quartz OSL is usually the preferred signal in sediment dating, it is often not sufficiently  
223 sensitive when measured in primary rocks (e.g. Sohbati et al., 2011; Guralnik et al., 2015). Thus, we  
224 made use of infrared stimulated luminescence (IRSL) signal to measure the solid rock slices. The IRSL  
225 signal originates almost entirely from feldspar grains in rock slices (e.g. Baril and Huntley, 2003).

226 Luminescence measurements were carried out using a Risø TL/OSL reader (model DA-20) with  
227 infrared light stimulation (870 nm,  $\sim 130 \text{ mW cm}^{-2}$ ) and photon detection through a Schott BG  
228 39/Corning 7-59 blue filter combination (2 and 4 mm, respectively). Beta irradiations used a calibrated

229  $^{90}\text{Sr}/^{90}\text{Y}$  source mounted on the reader delivering a dose rate of  $\sim 0.08 \text{ Gy s}^{-1}$  to the rock slices. The  
230 IRSL signal was measured using a conventional single-aliquot regenerative-dose (SAR) protocol. The  
231 residual natural signal ( $L_n$ ) and the subsequent response to a test dose ( $T_n$ ) from each slice were  
232 measured using an IRSL signal at  $50^\circ\text{C}$  ( $\text{IR}_{50}$ ) for 100 s (Wallinga et al., 2000). A pause of 30 s was  
233 inserted before the stimulation to make sure that all the grains within a slice reached the stimulation  
234 temperature. The same thermal pretreatment of  $250^\circ\text{C}$  for 100 s was applied before the natural and test  
235 dose measurements. Each cycle of the SAR protocol finished with an IR stimulation at  $290^\circ\text{C}$  for 100 s  
236 to minimize recuperation (Wallinga et al., 2007).

237 The radionuclide concentrations ( $^{238}\text{U}$ ,  $^{226}\text{Ra}$ ,  $^{232}\text{Th}$  and  $^{40}\text{K}$ ) were determined using high-resolution  
238 gamma spectrometry by measurement on a high-purity germanium detector for at least 24 h. Details of  
239 the gamma spectrometry calibration are given in Murray et al. (1987). To calculate the size-dependent  
240 internal beta dose rate from  $^{40}\text{K}$  in K-rich feldspar grains, a grain size and composition analysis was  
241 carried out, using scanning electron microscopy (SEM), on several slices from each rock to determine  
242 the average size of the constituent K-rich feldspar grains (Table 1S). Using the simplifying assumption  
243 that the grains are spherical with this dimension as the diameter, the beta dose rate contributions from  
244  $^{40}\text{K}$  and  $^{87}\text{Rb}$  were then calculated assuming a potassium content of  $12.5 \pm 0.5\%$  (Huntley and Baril,  
245 1997) and a  $^{87}\text{Rb}$  content of  $400 \pm 100 \text{ ppm}$  (Huntley and Hancock, 2001). A small internal alpha  
246 contribution of  $0.10 \pm 0.05 \text{ Gy ka}^{-1}$  from internal  $^{238}\text{U}$  and  $^{232}\text{Th}$  was also included in the dose rates,  
247 derived from  $^{238}\text{U}$  and  $^{232}\text{Th}$  concentration measurements by Mejdahl (1987). The radionuclide  
248 concentrations were converted to dose rate data using the conversion factors from Guérin et al. (2011).  
249 The contribution from cosmic radiation to the dose rate was calculated following Prescott and Hutton  
250 (1994), assuming an uncertainty of 5%. The water content is negligible. Radionuclide concentrations  
251 and infinite-matrix beta and gamma dose rates are summarized in Table S1.

252           **5. Results**

253           **5.1. Estimation of model parameters**

254           To derive the exposure age ( $t$ ) (Eqn. 4) or the erosion rate ( $\epsilon$ ) (Eqn. 8) by fitting the corresponding  
255 equations to luminescence-depth profiles, the values of other parameters in the models must be derived  
256 independently. This can be done either by derivation from first principles or by fitting the models to an  
257 appropriate calibration sample (Sohbati et al., 2011, 2012a, b). We next discuss the evaluation of the  
258 individual parameters:

259           *Dose rate* ( $\dot{D}$ ): Ideally, in order for the beta and gamma dose rates derived from gamma  
260 spectrometry to be applicable to the IRSL-depth profiles, they need to be modified to account for the  
261 deviation from the infinite-matrix assumption around the rock surface-air interface. However, as  
262 mentioned before, this is not relevant to our problem. In practice, the average linear beta attenuation  
263 coefficient in granitic rocks with a typical density of  $\sim 2.6 \text{ g.cm}^{-3}$  is  $\sim 1.9 \text{ mm}^{-1}$  (e.g. Sohbati et al.,  
264 2015). Hence the beta dose rate reaches  $\sim 98\%$  of the infinite matrix dose rate at a depth of  $\sim 2 \text{ mm}$  in  
265 our samples. Given that electron detrapping rate due to daylight bleaching at such depths (i.e.  $< 2 \text{ mm}$ )  
266 is much higher than electron trapping rate by dose rate, the effect of beta dose rate variation in the  
267 bleached part of the profile is negligible. The gradient of gamma dose rate with depth, on the other  
268 hand, is much less steep than that of beta (e.g. Aitken, 1985) and occurs over the entire length of the  
269 profiles measured here (i.e.  $\sim 3.5 \text{ cm}$ ). The gamma linear attenuation coefficient was calculated  
270 following Sohbati et al. (2015). The calculated coefficient is  $\sim 0.02 \text{ mm}^{-1}$ , which results in an increase  
271 of gamma dose rate by a factor of  $\sim 1.5$  from the surface to a depth of  $\sim 3.5 \text{ cm}$ ; however, on average,  
272 the gamma dose rate is only  $\sim 30\%$  of the total dose rate in our samples. Thus, there is only a weak  
273 variation of total dose rate with depth, which may be neglected for the benefit of simplification of the

274 model. The variation of cosmic dose rate due to the attenuation of cosmic rays into rocks was also  
275 calculated using the depth dependence model of Prescott and Hutton (1994). The resulting beta  
276 (including contributions from internal  $^{40}\text{K}$  and  $^{87}\text{Rb}$ ), gamma and cosmic dose rates were then summed  
277 and averaged over the length of each luminescence-depth profile to give the mean effective total dose  
278 rate in Eqns. (4) and (8) (Table 1).

279 *Characteristic dose ( $D_0$ ):* To estimate the value of  $D_0$  for each boulder, the dose-response curves of  
280 the surface and the deepest slice from one of the luminescence-depth profiles for each sample, were  
281 measured up to high doses (up to  $\sim 1000$  Gy, i.e. close to saturation). The resulting dose-response  
282 curves were then fitted with a single saturating exponential function to calculate the value of  $D_0$ .  
283 Although the resulting  $D_0$  values vary significantly from sample to sample, no systematic difference  
284 with depth within individual samples is observed. We therefore take an average of the two  $D_0$  values  
285 for each sample as the most representative value to be used in Eqns. (4) and (11) for the whole profile  
286 (Table 1).

287 *Luminescence decay rate ( $\overline{\sigma\phi_0}$ ) and light attenuation coefficient ( $\mu$ ):* As shown in Eqn. 2, the  
288 overall rate of charge detrapping  $E(x)$  ( $\text{ka}^{-1}$ ) (Eqn. 2) is a function of charge detrapping rate at the  
289 surface of the rock  $\overline{\sigma\phi_0}$  ( $\text{ka}^{-1}$ ) and the linear light attenuation coefficient  $\mu$  ( $\text{mm}^{-1}$ ) into the rock. These  
290 site-specific and material-dependent parameters can, in principle, be determined independently from  
291 first principles and/or by controlled field and laboratory measurements. However, earlier theoretically-  
292 derived values of  $\overline{\sigma\phi_0}$  have been shown to be orders of magnitude different from the empirically-  
293 derived values obtained by regression of the model to known-age calibration samples (Sohbati et al.,  
294 2011; 2012a), and no attempt to measure  $\mu$  in the laboratory has been reported. The alternative  
295 empirical approach is to quantify these parameters by fitting the model to a non-eroding known-age

296 calibration sample (Sohbati et al., 2012a). Such a surface was serendipitously created in one location by  
297 earlier workers collecting CN samples during an earlier field campaign in 2010 (sampling date given  
298 by Zhaode Yuan, personal communication) (Fig. 4). Fresh chisel marks on the surface of the boulder  
299 provide evidence that the surface has not eroded significantly during the known exposure period (~3  
300 years). We sampled two profiles within a few centimeters of each other; one was taken from the natural  
301 surface of the boulder, complete with varnish, and a second from the bottom of a > 2-cm deep chiseled  
302 surface (Fig. 4). A simple qualitative assessment shows that the signal resetting in the profile from the  
303 original surface with a  $^{10}\text{Be}$  age of 15.7 ka penetrates further into the rock than that in the core from the  
304 > 2-cm deep chisel mark (Fig. 4). This is in line with the prediction of the model that luminescence is  
305 reset deeper into the surface with longer exposure time. A further comparison between the two profiles  
306 shows that the piece removed in 2010 was almost certainly thick enough (> 2 cm) to eliminate the part  
307 of the profile that was bleached prior to CN sampling (i.e. < 2 cm, Fig. 4). We can thus be confident  
308 that the present-day shallow profile was saturated at the surface as a result of sampling three years ago  
309 (satisfying the condition of  $n = N$  at the beginning of the bleaching–irradiation process,  $t = 0$ ) and has  
310 not undergone any significant erosion during this period.

311 A visual inspection of the resetting fronts in the two profiles also reveals that they have similar  
312 curvature (Fig. 4; see also Fig. S1). According to the model, the gradient of luminescence-depth  
313 profiles is controlled by the attenuation of light into the surface ( $\mu$  in Eqn. 2). Given the material-  
314 dependent nature of this parameter and the similarity of the curvature of the two profiles, we assume  
315 that they have the same light attenuation coefficient (Fig. 4).

316 We fit the two datasets simultaneously by sharing  $\overline{\sigma\phi_0}$  and  $\mu$  between the profiles and replacing the  
317 length of exposure time  $t$  by three years in the model for the shallow profile. The 3-year old profile is

318 our reference data for calibration; it allows us to determine the values of the model parameters, and  
319 thereby, the apparent exposure time for the deeper profile (Figs. 4 and 5c). The best-fit values for  $\overline{\sigma\phi_0}$   
320 and  $\mu$  are  $2165\pm 51 \text{ ka}^{-1}$  and  $0.59\pm 0.01 \text{ mm}^{-1}$ , respectively. The apparent best-fit luminescence surface-  
321 exposure age for the deeper profile is  $2.5\pm 0.3 \text{ ka}$ , much younger than the  $^{10}\text{Be}$  exposure age of  $15.7 \text{ ka}$   
322 obtained from the same surface. This obvious age underestimation is presumed to arise from the effect  
323 of erosion on the luminescence-depth profile. Using the best-fit values for  $\overline{\sigma\phi_0}$  and  $\mu$  and setting the  
324 exposure time  $t$  to  $15.7 \text{ ka}$  results in a predicted luminescence profile that penetrates much deeper than  
325 that measured (Figs. 4 and 5c). This is the profile that would have developed in  $15.7 \text{ ka}$ , had there been  
326 no erosion. Similarly, we can model the secular-equilibrium profile ( $dn/dt = 0$ ) for zero erosion rate  
327 (Figs. 4 and 5c); it penetrates even deeper than the  $15.7 \text{ ka}$  profile. All three profiles are statistically  
328 distinguishable suggesting that in the absence of erosion a  $15.7 \text{ ka}$  profile could have been resolved  
329 from the secular-equilibrium profile.

## 330 **5.2. The effect of feldspar IRSL signal instability on the models**

331 Our models implicitly assume that the competition between electron trap filling by environmental  
332 radiation and trap emptying by optical bleaching in IRSL-depth profiles is governed by first-order  
333 kinetics. However, trapped electrons participating in IRSL often undergo localized recombination from  
334 the ground state and/or the excited state of the trap leading to signal instability (e.g., Huntley, 2006;  
335 Jain et al., 2015). Such a signal instability is expected to affect the shape of the luminescence-depth  
336 profile because recently-trapped charge (i.e. charge population far from field equilibrium; Lamothe et  
337 al., 2003) makes up a larger fraction of the total at low signal intensities (i.e. shallower depths) than at  
338 high signal intensities closer to saturation (i.e. deeper in the profile). Nonetheless, for our samples we  
339 assume we can ignore these effects in a first order approximation, because the apparent luminescence

340 ages (discussed below) are, with one exception, < 12 ka. On such timescales, any second order effects  
341 related to instability of the signal acquired due to ambient ionizing radiation is negligible compared to  
342 bleaching by daylight close to the surface.

343 To test the validity of this approximation, we have superimposed the bleaching profiles from the 3-  
344 year old calibration sample (Fig. 4, profile 1) with the profile from the adjacent natural surface  
345 presumed to have been exposed for 15.7 ka ( $^{10}\text{Be}$  age; Fig. 4, profile 2), by simply adding 12 mm to the  
346 depth scale of the 3-year old profile (see Fig. S1). The two profiles are now indistinguishable,  
347 confirming that any effect of signal instability on the shape of the profile is negligible over a timescale  
348 of up to ~16 ka.

### 349 **5.3. Apparent ages and erosion rates**

350 As presented earlier, we have two explicit models represented by two different analytical solutions:  
351 the age model (Eqn. 4; assumes no erosion and solves for exposure age) and the steady-state erosion  
352 rate model (Eqn. 8, assumes no age information and solves for erosion rate). In this section, we first  
353 apply the age model to all the luminescence-depth profiles and then the erosion rate model.

354 Figure 5 shows the IRSL-depth profiles measured into the 8 boulder surfaces. All the profiles have  
355 the characteristic sigmoidal shape as predicted by the model for constantly exposed surfaces; they start  
356 at negligible values at the surface and gently rise to saturation at depths > 20 mm. Given that all the  
357 samples were collected from the top flat surfaces of boulders from localities that are < 100 km apart  
358 within the valley, we assume that they have all been exposed to similar solar insolation ( $\varphi_0$ ). Also, it  
359 has been shown that feldspars of different compositions have similar bleaching response (Spooner,  
360 1994) and so similar optical cross sections ( $\sigma$ ). Thus, one can assume that all our samples have the  
361 same value of  $\overline{\sigma\varphi_0}$  as determined above from the calibration sample. On the other hand,  $\mu$  is a sample-

362 dependent parameter that can vary from one rock to another. Accordingly, we simultaneously fit Eqn. 4  
363 to all the profiles, sharing  $\overline{\sigma\varphi_0}$  ( $2165\pm 51 \text{ ka}^{-1}$ , derived from the calibration sample) between all the fits,  
364 but leaving  $\mu$  a free parameter.

365 Figure 5 shows the resulting best fits and the apparent luminescence surface-exposure ages for all  
366 the boulders. The corresponding values of  $\mu$  are summarized in Table 1. The apparent luminescence  
367 age of sample MUST10-1 is  $11.6\pm 2.3 \text{ ka}$  which is comparable with the  $^{10}\text{Be}$  age of  $9.9\pm 0.9 \text{ ka}$  obtained  
368 from the same surface (Fig. 5a). Also, boulder XJ64-1 has a minimum age of  $36.4\pm 2.1 \text{ ka}$  constrained  
369 by our  $1/\mu$  (mm) limit on the penetration depth of the  $x_{50\%}$ ; this minimum age is consistent with the  
370  $^{10}\text{Be}$  age of  $86.4\pm 8.3 \text{ ka}$  for this boulder (Fig. 5h). For all the other samples however, the apparent  
371 luminescence surface exposure ages are significantly younger than the corresponding  $^{10}\text{Be}$  ages. This  
372 systematic underestimation in apparent luminescence exposure ages suggests that the profiles in these  
373 boulders are either in secular equilibrium or have been affected by erosion. To investigate this, a  
374 similar approach as was used with the calibration sample was adopted; we assume no erosion, and  
375 model two profiles for each sample by setting the exposure time to the  $^{10}\text{Be}$  age of the sample or to  
376 infinity (Fig. 5).

377 As mentioned above, the apparent luminescence exposure age of sample MUST10-1 is comparable  
378 to its  $^{10}\text{Be}$  age. As a result, the predicted profile corresponding to the  $^{10}\text{Be}$  age in sample MUST10-1 is  
379 indistinguishable from the best fit of the model to the data, whereas the predicted secular-equilibrium  
380 profile is discernibly deeper (Fig. 5a). Also, in case of XJ64-1, the predicted steady-state and the fitted  
381 age model profiles are identical and deeper than the predicted  $^{10}\text{Be}$  profile, indicating that this sample  
382 must be in secular equilibrium (Fig. 5h). Except for MUST10-1 and XJ64-1, the predicted  $^{10}\text{Be}$ -  
383 equivalent and steady-state resetting profiles in all the other boulders penetrate to greater depths than

384 the observed profiles, suggesting that the measured profiles are distinct and far from secular  
385 equilibrium; they must therefore have been affected by erosion (Fig. 5).

386 Given that erosion has most likely played a significant role in the development of the IRSL-depth  
387 profiles, we now test whether our data can be explained by the erosion rate model (Eqn. 8). As with  
388 Eqn. 4, we simultaneously fit Eqn. 8 to all the profiles, sharing  $\overline{\sigma\phi_0}$  ( $2165\pm 51 \text{ ka}^{-1}$ , derived from the  
389 calibration sample) between all the fits, but leaving  $\mu$  a free parameter. Figure 5 shows that the model  
390 provides excellent fits to the data from all the samples; the fits are indistinguishable from and so  
391 superimpose those obtained using the age model (i.e. without erosion; Fig. 5). The resulting values of  $\mu$   
392 are summarized in Table 1. These are also indistinguishable from those derived using Eqn. 4 (Table 1);  
393 this is not surprising since  $\mu$  is a material-dependent parameter and should not be dependent on age or  
394 erosion rate (see also Fig. S2 and associated text). The apparent erosion rates derived from Eqn. 8 vary  
395 from  $< 0.038\pm 0.002 \text{ mm ka}^{-1}$  for sample XJ64-1 to  $444\pm 12 \text{ mm ka}^{-1}$  for sample XJ64 (Table 1).

## 396 **6. Discussion**

397 The apparent luminescence surface-exposure age of sample MUST10-1 is  $11.6\pm 2.3 \text{ ka}$  which,  
398 within error limits, is in agreement with the  $^{10}\text{Be}$  age of  $9.9\pm 0.9 \text{ ka}$  obtained from the same surface  
399 (Fig. 5a). This is the first time that a luminescence surface exposure age has been verified using  
400 independent age control. Given that luminescence-depth profiles are much more susceptible to the  
401 effect of erosion than CN-depth profiles, the agreement between the two ages implies a low rate of  
402 erosion for the surface of this boulder. The application of the erosion rate model indeed confirms this  
403 implication, as it yields an apparent luminescence erosion rate of  $0.09\pm 0.02 \text{ mm ka}^{-1}$  (Fig. 5a).

404 Boulder XJ64-1 with a  $^{10}\text{Be}$  age of  $86.4\pm 8.3 \text{ ka}$  has a minimum luminescence age of  $36.4\pm 2.1 \text{ ka}$   
405 (Fig. 5h). The fact that the observed profile is consistent with the expected profile in secular

406 equilibrium assuming no erosion, suggests a negligible erosion of the surface of XJ64-1 (Fig. 5h). This  
407 suggestion is further confirmed by the application of erosion rate model, which results in a maximum  
408 apparent erosion rate of  $0.038 \pm 0.002 \text{ mm ka}^{-1}$  (Fig. 5h). The surface of boulder XJ64-1 currently lies  
409 only a few centimetres above the ground (Fig. 3h) and thus any effect of wind abrasion at its surface  
410 must be limited (Shao, 2009). The abundant desert varnish on the surface of this boulder (Fig. 3h) also  
411 argues for an absence of significant erosion, indicating that within the geological context, the very low  
412 erosion rate obtained here is plausible. Nevertheless, given the size and position of the boulder in the  
413 landscape, we cannot completely rule out occasional burial deep enough to shield it from daylight, but  
414 not from the cosmic rays. In such a scenario, the effective value of  $\overline{\sigma\phi_0}$  would be smaller than that for  
415 the calibration sample. However, any decrease in the effective  $\overline{\sigma\phi_0}$  value would only bring the  
416 equilibrium profile to depths shallower than we observe. Based on our fitting results we can conclude  
417 that the cover could have never been more than ~46% (minimum luminescence age/ $^{10}\text{Be}$  age) of the  
418 total time since the emplacement of the boulder.

419 In contrast to XJ64-1, the nearby large boulder (XJ64) has an anomalously high apparent erosion  
420 rate of  $444 \pm 12 \text{ mm ka}^{-1}$  (Fig. 5g), which is several orders of magnitude larger than those obtained for  
421 the other boulders in this study. The surface of XJ64 has visibly undergone considerable erosion  
422 compared to the other boulders, as evidenced by its rough, unvarnished surface (see also Fig. 3).  
423 Nevertheless, steady-state erosion at such a high rate seems very unlikely in an environment where it is  
424 expected that wind abrasion dominates (Portenga and Bierman, 2011). In addition, the boulder has been  
425 exposed for ~70 ka, and this would imply a loss of > 3 m, making the CN age a serious underestimate  
426 and the total loss even greater. A more likely explanation is that the observed profile was inadvertently  
427 sampled from a location where there had been a discrete loss of material, e.g. by freeze/thaw flaking.

428 We also note that the value of  $\mu$  for this boulder ( $0.2 \text{ mm}^{-1}$ ) is  $\sim 3$  times smaller than any of the values  
429 obtained for the other boulders, and this may reflect some undetected failure of the application of the  
430 model to this sample.

431 Finally, the observed marked variability in surface loss, as evidenced by apparent surface roughness  
432 in the field (Fig. 3), implies that the luminescence erosion rates derived here from such smooth  
433 varnished spots must be regarded as minimum estimates of rock surface erosion rates in the Eastern  
434 Pamirs, China. The observation of a significant varnish patina on surfaces probably eroding at  $> 0.1$  to  
435  $2 \text{ mm ka}^{-1}$  suggests that the varnish accumulation rates at the Eastern Pamirs must be higher than the  
436 fastest rates of  $\sim 600 \text{ } \mu\text{m ka}^{-1}$  previously documented in southwestern United States (Spilde et al.,  
437 2013).

#### 438 **6.1. Luminescence-depth profile: chronometer or erosion-meter?**

439 In order to discuss the information available in a luminescence-depth profile, we first simulate the  
440 behavior of the erosion rate model (Eqn. 8) for erosion rates of 0 and  $1.5 \text{ mm ka}^{-1}$ . The model profiles  
441 are first generated by setting  $t$  in Eqn. 4 to a known age (i.e. from 0.1 a to 100 ka) and then fitted by  
442 Eqn. (8) using the appropriate erosion rate. The other model parameters (i.e.  $\dot{D}$ ,  $D_o$ ,  $\overline{\sigma\varphi_0}$  and  $\mu$ ) are  
443 assigned values comparable to those obtained for our samples. Figure 6a plots, against exposure time,  
444 the product of the  $x_{50\%}$  of the resulting model profiles and  $\mu$ ; this gives a material independent,  
445 dimensionless parameter which quantifies the depth, in multiples of the mean free path, at which  
446 luminescence reaches 50% of its saturation value. We define the extrapolation of the horizontal  
447 (steady-state) part of the  $1.5 \text{ mm ka}^{-1}$  curve to the zero erosion rate curve to be the equilibrium age limit  
448 (i.e.  $\sim 1 \text{ ka}$ ) recorded by a profile eroding at  $1.5 \text{ mm ka}^{-1}$  (Fig. 6a). In a surface that has been exposed  
449 for a period much shorter than  $\sim 1 \text{ ka}$ , the luminescence-depth profile is primarily a chronometer,

450 because over this time span, the rate of migration of  $x_{50\%}$  into the rock is much greater than the rate of  
451 removal of grains from the surface of the rock (Fig. 6a). Thus, a profile in this time zone can be fitted  
452 by Eqn. 4 to determine the apparent exposure age of the surface. On the other hand, at times much  
453 longer than the equilibrium age limit, the luminescence-depth profile is essentially an erosion-meter,  
454 because it is in erosional steady state and has no memory of the exposure time. A profile in this time  
455 zone can be modelled using Eqn. 8 to derive the erosion rate. There remains an intermediate transition  
456 interval ( $\sim 0.3$  to  $\sim 3$  ka, points A and B in Fig. 6a) during which the luminescence-depth profile evolves  
457 from being a chronometer to an erosion-meter. In order to derive either the apparent exposure age or  
458 erosion rate in this transition period, a knowledge of the other parameter is required. In other words, to  
459 determine the apparent exposure age from a profile in this time zone, the erosion rate must be known  
460 independently, and vice versa.

461 In order to determine the equilibrium age range for various erosion rates, we have also simulated the  
462 behavior of the erosion rate model (Eqn. 8) for a range of erosion rates from 0 to 1500 mm ka<sup>-1</sup>. In  
463 Figure 6b, the equilibrium ages for individual erosion rates are extrapolated onto the zero erosion rate  
464 curve. For the erosion rates relevant to our samples (0.015 to 1.5 mm ka<sup>-1</sup>), luminescence-depth profiles  
465 reach equilibrium after 44 to 1 ka of exposure. These equilibrium age limits define the timescale to  
466 which the corresponding erosion rates refer. For instance, an erosion rate of 0.015 mm ka<sup>-1</sup> is  
467 effectively averaged over the last 44 ka of surface exposure whereas an erosion rate of 1.5 mm ka<sup>-1</sup> is  
468 only averaged over the last 1 ka. These luminescence-depth profiles have no memory of the erosion  
469 history prior to these age limits.

470 Depending on the parameter values and the depth resolution, the  $1/\mu$  constraint can limit either the  
471 minimum apparent exposure age or the maximum apparent erosion rate that can be derived from a

472 luminescence-depth profile. The typical value of  $\mu$  in our samples is between 0.5 and 1 mm<sup>-1</sup> (Fig. 5),  
473 meaning that the  $x_{50\%}$  point in the deepest profiles that can be reliably distinguished from the  
474 bleaching/dose-rate steady-state profile must lie at least 1–2 mm shallower than the corresponding  
475 point in the steady-state profile. Given the current resolution of sampling (i.e. slicing at 1.5 mm depth  
476 intervals) and samples with typical parameter values, profiles with an apparent exposure age < 1 a or an  
477 apparent erosion rate > 1500 mm ka<sup>-1</sup> (see Fig. 6) cannot be modelled reliably as these would be  
478 indistinguishable from steady-state. Collection of high-resolution data using spatially-resolved  
479 luminescence imaging techniques (e.g. Greilich and Wagner, 2006) may help to overcome this  
480 limitation in the future.

## 481 **7. Conclusion**

482 We have further developed the luminescence-surface exposure dating technique (Sohbati et al.,  
483 2012a,b) by taking the effect of rock surface erosion into account. The new model presented here (Eqn.  
484 8) has been fitted to luminescence-depth profiles measured in subaerially exposed rock surfaces to give  
485 centennial- to millennial-scale (10<sup>2</sup>–10<sup>4</sup> years) hard rock erosion rates. The model predicts that the  
486 higher the erosion rate, the faster a luminescence-depth profile changes from being a (surface exposure)  
487 chronometer to an erosion rate meter. For example, for an erosion rate of 1.5 mm ka<sup>-1</sup> it takes only ~3  
488 ka for a profile to become useful for deriving a unique erosion rate.

489 The application of the new model has been tested by fitting the IRSL-depth profiles measured into  
490 several glacial and landslide boulders in the Eastern Pamirs, China. The derived erosion rates for 7 out  
491 of the 8 boulders sampled in this study vary between < 0.038±0.002 and 1.72±0.04 mm ka<sup>-1</sup> (the eighth  
492 boulder gave an anomalously high erosion rate, possibly due to a recent chipping/cracking loss of  
493 surface). In the case of one sample with a low erosion rate of 0.09±0.02 mm ka<sup>-1</sup>, we obtained an

494 apparent luminescence surface exposure age of  $11.6 \pm 2.3$  ka, consistent with the  $^{10}\text{Be}$  age of  $9.9 \pm 0.9$  ka  
495 for the same surface. This is the first time that a luminescence surface exposure age has been verified  
496 by an independent age control.

497 Unfortunately, in the absence of an independent method that enables the measurement of erosion  
498 rates over similar timescales (i.e.  $10^2$ – $10^4$  years), we cannot make any direct comparison between the  
499 rates measured here and those estimated using other techniques in the literature. It is however  
500 noteworthy that these luminescence erosion rates are only comparable with long-term CN erosion rates  
501 reported for the most-slowly eroding outcrops in polar climates with a median erosion rate of  $\sim 1 \text{ m Ma}^{-1}$   
502 <sup>1</sup> (Portenga and Bierman, 2011). One can speculate that the lower centennial- to millennial-scale  
503 luminescence erosion rates derived here, when compared to the more typical CN rates measured in  
504 non-polar environments (Portenga and Bierman, 2011), may reflect the deceleration of erosion rates  
505 during the Holocene. However, any solid conclusion of this nature requires many more measurements  
506 of luminescence erosion rates in different environments and lithologies.

## 507 **Acknowledgements**

508 This work was financially supported by the Aarhus University Research Foundation (AUFF  
509 Pilotcenter for Quantitative Earth Surface Studies), the Carlsberg Foundation (Grant no. 2012\_01  
510 \_0838), the National Natural Science Foundation of China (Grant no.: 41472161), and the State Key  
511 Laboratory of Earthquake Dynamics (Grant no.: LED2013A09). BG was supported by the Netherlands  
512 Organisation for Scientific Research (NWO) VENI grant 863.15.026. We would like to thank Dr.  
513 Zhaode Yuan for providing us with his field photo of sample Muztagh–2. We thank Dr Nathan Brown  
514 for the careful review of the manuscript.

515

## Appendix A

516

Consider Eqn. (7) from the main text:

$$\frac{dn}{dt} = (N - n)F - nE_0 e^{\mu \varepsilon t} \quad (7)$$

517

To solve Eqn. (7), we introduce  $\tau = (\mu \varepsilon)^{-1}$  and make use of dimensionless variables  $r = n/N$ ,

518

$a = F\tau$  and  $v = E(x(t))\tau = \tau E_0 \exp(t/\tau) = v_0 \exp(t/\tau)$ , whose substitution into Eqn. (7) yields:

$$\frac{dr}{dt} = \frac{a}{\tau}(1 - r) - \frac{v}{\tau}r \quad (A.1)$$

519

Dividing both sides of Eqn. (A.1) by the identity  $dv/dt = v/\tau$  and rearranging results in:

$$\frac{dr}{dv} + r\left(\frac{a}{v} + 1\right) = \frac{a}{v} \quad (A.2)$$

520

Eq. (A.2) is a first order non-homogeneous differential equation. Recast as  $dr/dv + f(r)r = g(r)$ , it

521

has a general solution  $r = e^{-\int f(r)dx} \left\{ \int e^{\int f(r)dx} g(r)dr + C \right\}$ . Substituting  $f(r) = a/v + 1$ ,  $g(r) =$

522

$a/v$ , and integrating, we obtain:

$$r = av^{-a} e^{-v} \int_{v_0}^v u^{a-1} e^u du \quad (A.3)$$

523

where  $u$  is a dummy integration variable. To obtain an analytical solution for Eqn. (A.3), we start with

524

the simple case of  $v_0 = 0$  at  $t = 0$ , i.e. an initially negligible optical loss coefficient in Eqn. (7) in a

525

mineral that is initially fully shielded from light. Using a power series to expand  $e^u$  in the integrand,

526

we integrate and rearrange Eqn. (A.3) as follows:

$$\begin{aligned}
r(v) &= av^{-a}e^{-v} \int_0^v u^{a-1} \left(1 + \frac{u}{1!} + \frac{u^2}{2!} + \dots\right) du = av^{-a}e^{-v} \left(\frac{v^a}{a} + \frac{v^{a+1}}{(a+1)1!} + \frac{v^{a+2}}{(a+2)2!} + \dots\right) \\
&= e^{-v} \left(1 + \frac{a}{(a+1)1!}v + \frac{a}{(a+2)2!}v^2 + \dots\right) \\
&= e^{-v} \left(1 + \frac{a}{(a+1)1!}v + \frac{a(a+1)}{(a+1)(a+2)2!}v^2 + \dots\right) \tag{A.4}
\end{aligned}$$

527 Making the substitutions  $z = v$ ,  $m = a$  and  $n = a + 1$ , we notice that the power series in Eqn. (A.4)  
528 conforms to the confluent hypergeometric function (Abramowitz and Stegun, 1964):

$$M(m, n, z) = \left(1 + \frac{m}{n \cdot 1!}z + \frac{m(m+1)}{n(n+1)2!}z^2 + \dots\right) \tag{A.5}$$

529 which efficiently reduces Eqn. (A.4) to:

$$r(v) = e^{-v}M(a, a+1, v) \tag{A.6}$$

530 To further simplify Eqn. (A.6), we apply Kummer's theorem  $M(m, n, z) = e^z M(n-m, n, -z)$ , which  
531 reduces Eqn. (A.6) to the desired form:

$$r(v) = M(1, 1+a, -v) \tag{A.7}$$

532 Remembering that  $\tau = (\mu\varepsilon)^{-1}$ , by substituting the dimensionless variables by physical variables, i.e.  
533  $r = n/N$ ,  $a = F\tau$ , and  $v = E(x)\tau$  into Eqn. (A.7), for  $x = x_0 - \varepsilon t$  we obtain:

$$\frac{n(x, \varepsilon)}{N} = M\left(1, 1 + \frac{F}{\mu\varepsilon}, \frac{-E(x)}{\mu\varepsilon}\right) \tag{A.8}$$

534 which is the same as Eqn. (8) in the main text, and describes luminescence systems exhuming towards  
535 the present-day surface from initially photon-impenetrable depths ( $E_0 = 0$ ). The confluent  
536 hypergeometric function  $M(m, n, z)$  is readily available in all common modelling software, either as an  
537 in-built function (e.g. Matlab, Mathematica) or as an optional extension (e.g. Excel, OriginLab). If

538 nevertheless in need to numerically evaluate  $M(m, n, z)$  using series expansion, consult Abramowitz  
 539 and Stegun (1964).

540 The treatment can be further extended to include an arbitrary  $E_0 \geq 0$ , i.e. an initial boundary  
 541 condition  $0 \leq v_0 < v$ . To do this, we first expand Eqn. (A.3) into:

$$r = av^{-a}e^{-v} \int_{v_0}^v u^{a-1} e^u du = av^{-a}e^{-v} \int_0^v u^{a-1} e^u du - av^{-a}e^{-v} \int_0^{v_0} u^{a-1} e^u du \quad (\text{A.9})$$

542 We now use the previously-derived identity (Eqns. A.3 and A.7):

$$av^{-a}e^{-v} \int_0^v u^{a-1} e^u du = M(1, 1 + a, -v)$$

543 to express the last integral in Eqn. (A.9) as:

$$\int_0^{v_0} u^{a-1} e^u du = a^{-1}v_0^a e^{v_0} M(1, 1 + a, -v_0)$$

544 By substitution of the two identities above in to Eqn. (A.9), we obtain the desired form:

$$\begin{aligned} r(v) &= M(1, 1 + a, -v) - av^{-a}e^{-v} [a^{-1}v_0^a e^{v_0} M(1, 1 + a, -v_0)] \\ 545 \quad &= M(1, 1 + a, -v) - (v_0/v)^a e^{v_0-v} M(1, 1 + a, -v_0) \end{aligned} \quad (\text{A.10})$$

546           **References**

- 547   Abramowitz, M., Stegun, I., 1964. Handbook of mathematical functions: with formulas, graphs, and  
548   mathematical tables. Vol. 55. Courier Corporation.
- 549   Aitken, M.J., 1985. Thermoluminescence dating, Studies in Archaeological Science.
- 550   Aitken, M.J., 1998. An introduction to optical dating: The dating of Quaternary sediments by the use of  
551   photon-stimulated luminescence, Oxford science publications. doi:10.1002/(SICI)1520-  
552   6548(200001)15:1<81::AID-GEA5>3.3.CO;2-Y
- 553   Balco, G., Stone, J.O., Lifton, N.A., Dunai, T.J., Lifton, A., Dunai, T.J., 2008. A complete and easily  
554   accessible means of calculating surface exposure ages or erosion rates from  $^{10}\text{Be}$  and  $^{26}\text{Al}$   
555   measurements. *Quat. Geochronol.* 3, 174–195. doi:10.1016/j.quageo.2007.12.001
- 556   Baril, M.R., Huntley, D.J., 2003. Infrared stimulated luminescence and phosphorescence spectra of  
557   irradiated feldspars. *J. Phys. Condens. Matter* 15, 8029–8048. doi:10.1088/0953-8984/15/46/018
- 558   Borchers, B., Marrero, S., Balco, G., Caffee, M., Goehring, B., Lifton, N., Nishiizumi, K., Phillips, F.,  
559   Schaefer, J., Stone, J., 2016. Geological calibration of spallation production rates in the CRONUS-  
560   Earth project. *Quat. Geochronol.* 31, 188–198. doi:10.1016/j.quageo.2015.01.009
- 561   Braun, J., Van Der Beek, P., Batt, G., 2006. Quantitative thermochronology: numerical methods for the  
562   interpretation of thermochronological data. Cambridge University Press.

563 Gardner, T.W., Jorgensen, D.W., Shuman, C., Lemieux, C.R., 1987. Geomorphic and tectonic process  
564 rates: effects of measured time interval. *Geology* 15, 259–261. doi:10.1130/0091-  
565 7613(1987)15<259:GATPRE>2.0.CO

566 Greilich, S., Wagner, G.A., 2006. Development of a spatially resolved dating technique using HR-OSL.  
567 *Radiat. Meas.* 41, 738–743. doi:10.1016/j.radmeas.2006.05.022

568 Guérin, G., Mercier, N., Adamiec, G., 2011. Dose-rate conversion factors: update. *Anc. TL* 29, 5–8.

569 Guralnik, B., Jain, M., Herman, F., Paris, R.B., Harrison, T.M., Murray, A.S., Valla, P.G., Rhodes,  
570 E.J., 2013. Effective closure temperature in leaky and/or saturating thermochronometers. *Earth Planet.*  
571 *Sci. Lett.* 384, 209–218. doi:10.1016/j.epsl.2013.10.003

572 Guralnik, B., Ankjærgaard, C., Jain, M., Murray, A.S., Müller, a., Wälle, M., Lowick, S.E., Preusser,  
573 F., Rhodes, E.J., Wu, T.-S., Mathew, G., Herman, F., 2015. OSL-thermochronometry using bedrock  
574 quartz: A note of caution. *Quat. Geochronol.* 25, 37–48. doi:10.1016/j.quageo.2014.09.001

575 Habermann, J., Schilles, T., Kalchgruber, R., Wagner, G.A., 2000. Steps towards surface dating using  
576 luminescence. *Radiat. Meas.* 32, 847–851. doi:10.1016/S1350-4487(00)00066-4

577 Huntley, D.J., Hancock, G.V., 2001. The Rb contents of the K-feldspar grains being measured in  
578 optical dating. *Anc. TL* 19, 43–46.

579 Huntley, D.J., 2006. An explanation of the power-law decay of luminescence. *J. Phys. Condens. Matter*  
580 18, 1359–1365. doi:10.1088/0953-8984/18/4/020

581 Kirchner, J.W., Finkel, R.C., Riebe, C.S., Granger, D.E., Clayton, J.L., King, J.G., Megahan, W.F.,  
582 Sites, F., 2001. Mountain erosion over 10 yr, 10 k.y., and 10 m.y. time scales. *Geology* 29, 591–594.  
583 doi:10.1130/0091-7613(2001)029<0591:MEOYKY>2.0.CO;2

584 Koppes, M.N., Montgomery, D.R., 2009. The relative efficacy of fluvial and glacial erosion over  
585 modern to orogenic timescales. *Nat. Geosci.* 2, 644–647. doi:10.1038/ngeo616

586 Lal, D., 1991. Cosmic ray labeling of erosion surfaces: in situ nuclide production rates and erosion  
587 models. *Earth Planet. Sci. Lett.* 104, 424–439. doi:10.1016/0012-821X(91)90220-C

588 Lal, D., Gallup, C.D., Somayajulu, B.L.K., Vacher, L., Caffee, M.W., Jull, A.J.T., Finkel, R.C., Speed,  
589 R.C., Winter, A., 2005. Records of cosmogenic radionuclides  $^{10}\text{Be}$ ,  $^{26}\text{Al}$  and  $^{36}\text{Cl}$  in corals: First studies  
590 on coral erosion rates and potential of dating very old corals. *Geochim. Cosmochim. Acta* 69, 5717–  
591 5728. doi:10.1016/j.gca.2005.08.012

592 Lamothe, M., Auclair, M., Hamzaoui, C., Huot, S., 2003. Towards a prediction of long-term anomalous  
593 fading of feldspar IRSL. *Radiat. Meas.* 37, 493–498. doi:10.1016/S1350-4487(03)00016-7

594 Laskaris, N., Liritzis, I., 2011. A new mathematical approximation of sunlight attenuation in rocks for  
595 surface luminescence dating. *J. Lumin.* 131, 1874–1884. doi:10.1016/j.jlumin.2011.04.052

596 Lehmann, B., Valla, P.G., King, G.E., Herman, F., 2018. Investigation of OSL surface exposure dating  
597 to reconstruct post-LIA glacier fluctuations in the French Alps (Mer de Glace, Mont Blanc massif).  
598 *Quat. Geochronol.* 44, 63–74. doi:10.1016/j.quageo.2017.12.002

599 Liu, J., Sohbaty, R., Murray, A.S., Jain, M., Andersen, J.L., Egholm, D.L., Linge, H., Chen, J., Luo, M.,  
600 Zheng, R., in review. Luminescence rock-surface dating reveals complex depositional histories of  
601 glacial and landslide boulders. *Earth Planet. Sci. Lett.*

602 Mejdahl, V., 1987. Internal radioactivity in quartz and feldspar grains. *Anc. TL* 5, 10–17.

603 Moses, C., Robinson, D., Barlow, J., 2014. Methods for measuring rock surface weathering and  
604 erosion: A critical review. *Earth-Science Rev.* 135, 141–161. doi:10.1016/j.earscirev.2014.04.006

605 Murray, A.S., Marten, R., Johnson, A., Martin, P., 1987. Analysis for naturally-occurring radionuclides  
606 at environmental concentrations by gamma spectrometry. *J. Radioanal. Nucl. Chem.* 115, 263–288.

607 Nishiizumi, K., Lal, D., Klein, J., Middleton, R., Arnold, J., 1986. Production of  $^{10}\text{Be}$  and  $^{26}\text{Al}$  by  
608 cosmic rays in terrestrial quartz in-situ and implications for erosion rates. *Nature* 319, 134–136.  
609 doi:<http://dx.doi.org/10.1038/319134a0>

610 Owen, L.A., Chen, J., Hedrick, K.A., Caffee, M.W., Robinson, A.C., Schoenbohm, L.M., Yuan, Z., Li,  
611 W., Imrecke, D.B., Liu, J., 2012. Quaternary glaciation of the Tashkurgan Valley, Southeast Pamir.  
612 *Quat. Sci. Rev.* 47, 56–72. doi:10.1016/j.quascirev.2012.04.027

613 Pederson, J.L., Chapot, M.S., Simms, S.R., Sohbaty, R., Rittenour, T.M., Murray, A.S., Cox, G., 2014.  
614 Reply to Simon and Reed: Independent and converging results rule out historic disturbance and  
615 confirm age constraints for Barrier Canyon rock art. *Proc. Natl. Acad. Sci.* 111, E5604–E5604.  
616 doi:10.1073/pnas.1421319112

617 Portenga, E.W., Bierman, P.R., 2011. Understanding earth's eroding surface with  $^{10}\text{Be}$ . *GSA Today* 21,  
618 4–10. doi:10.1130/G1111A.1

619 Prescott, J.R., Hutton, J.T., 1994. Cosmic ray contributions to does rates for Luminescence and ESR  
620 dating: large depths and long-terms variations. *Radiat. Meas.* 23, 497–500.

621 Sanderson, D., Smillie, M., McCullagh, R., Feathers, J., Hauser, N., 2011. Surface exposure dating by  
622 luminescence: developing and testing models for surface bleaching rates and erosion rates. 13th  
623 International Conference on Luminescence and Electron Spin Resonance Dating, 10-14 July 2011,  
624 Toruń, Poland, Book of Abstracts, p. 178.

625 Schumm, S.A., Lichty, R.W., 1965. Time, space, and causality in geomorphology. *Am. J. Sci.*  
626 doi:10.2475/ajs.263.2.110

627 Seong, Y.B., Owen, L.A., Yi, C., Finkel, R.C., 2009a. Quaternary glaciation of Muztag Ata and  
628 Kongur Shan: Evidence for glacier response to rapid climate changes throughout the late glacial and  
629 holocene in westernmost Tibet. *Bull. Geol. Soc. Am.* 121, 348–365. doi:10.1130/B26339.1

630 Seong, Y.B., Owen, L. A., Yi, C., Finkel, R.C., Schoenbohm, L., 2009b. Geomorphology of  
631 anomalously high glaciated mountains at the northwestern end of Tibet: Muztag Ata and Kongur Shan.  
632 *Geomorphology* 103, 227–250. doi:10.1016/j.geomorph.2008.04.025

633 Shao, Y., 2009. *Physics and Modelling of Wind Erosion*, Physics and Modelling of Wind Erosion.  
634 Springer Netherlands, Dordrecht. doi:10.1007/978-1-4020-8895-7\_4

635 Sohhati, R., Murray, A.S., Jain, M., Buylaert, J.-P., Thomsen, K.J., 2011. Investigating the resetting of  
636 OSL signals in rock surfaces. *Geochronometria* 38, 249–258. doi:10.2478/s13386-011-0029-2

637 Sohhati, R., Murray, A.S., Chapot, M.S., Jain, M., Pederson, J., 2012a. Optically stimulated  
638 luminescence (OSL) as a chronometer for surface exposure dating. *J. Geophys. Res.* 117, B09202.  
639 doi:10.1029/2012JB009383

640 Sohhati, R., Jain, M., Murray, A., 2012b. Surface exposure dating of non-terrestrial bodies using  
641 optically stimulated luminescence: A new method. *Icarus* 221, 160–166.

642 Sohhati, R., Murray, A.S., Buylaert, J.-P., Almeida, N. A. C., Cunha, P.P., 2012c. Optically stimulated  
643 luminescence (OSL) dating of quartzite cobbles from the Tapada do Montinho archaeological site  
644 (east-central Portugal). *Boreas* 41, 452–462. doi:10.1111/j.1502-3885.2012.00249.x

645 Sohhati, R., Murray, A.S., Porat, N., Jain, M., Avner, U., 2015. Age of a prehistoric “Rodedian” cult  
646 site constrained by sediment and rock surface luminescence dating techniques. *Quat. Geochronol.* 30,  
647 90–99. doi:10.1016/j.quageo.2015.09.002

648 Spilde, M.N., Melim, L.A., Northup, D.E., Boston, P.J., 2013. Anthropogenic lead as a tracer of rock  
649 varnish growth: Implications for rates of formation. *Geology* 41, 263–266. doi:10.1130/G33514.1

650 Stone, J.O., 2000. Air pressure and cosmogenic isotope production. *J. Geophys. Res.* 105759, 753–23.  
651 doi:10.1029/2000JB900181

652 Stephenson, W.J., Finlayson, B.L., 2009. Measuring erosion with the micro-erosion meter—  
653 Contributions to understanding landform evolution. *Earth-Science Rev.* 95, 53–62.  
654 doi:10.1016/j.earscirev.2009.03.006

655 Turowski, J.M., Cook, K.L., 2017. Field techniques for measuring bedrock erosion and denudation.  
656 *Earth Surf. Process. Landforms* 42, 109–127. doi:10.1002/esp.4007

657 Xu, X., Yi, C., 2014. Little Ice Age on the Tibetan Plateau and its bordering mountains: Evidence from  
658 moraine chronologies. *Glob. Planet. Change* 116, 41–53. doi:10.1016/j.gloplacha.2014.02.003

659 Yuan, Z., Chen, J., Owen, L.A., Hedrick, K.A., Caffee, M.W., Li, W., Schoenbohm, L.M., Robinson,  
660 A.C., 2013. Nature and timing of large landslides within an active orogen, eastern Pamir, China.  
661 *Geomorphology* 182, 49–65. doi:10.1016/j.geomorph.2012.10.028

662 Viles, H.A., 2001. Scale issues in weathering studies. *Geomorphology* 41, 63–72. doi:10.1016/S0169-  
663 555X(01)00104-0

664 Wallinga, J., Murray, A., Wintle, A., 2000. The single-aliquot regenerative-dose (SAR) protocol  
665 applied to coarse-grain feldspar. *Radiat. Meas.* 32, 529–533. doi:10.1016/S1350-4487(00)00091-3

666 Wallinga, J., Bos, A.J.J., Dorenbos, P., Murray, A.S., Schokker, J., 2007. A test case for anomalous  
667 fading correction in IRSL dating. *Quat. Geochronol.* 2, 216–221. doi:10.1016/j.quageo.2006.05.014

668 Warke, P.A., McKinley, J.M., 2011. Scale issues in geomorphology. *Geomorphology* 130, 1–4.  
669 doi:10.1016/j.geomorph.2011.04.031

670 Wintle, A., Murray, A.S., 2006. A review of quartz optically stimulated luminescence characteristics  
671 and their relevance in single-aliquot regeneration dating protocols. *Radiat. Meas.* 41, 369–391.  
672 doi:10.1016/j.radmeas.2005.11.001

673

### Figure captions

674 **Figure 1)** Model luminescence-depth profiles as predicted by Eqns (4) and (8) for (a) a non-eroding  
675 and (b) an eroding rock surface, respectively. The selected parameter values are  $\dot{D} = 6 \text{ Gy ka}^{-1}$ ,  $D_o =$   
676  $250 \text{ Gy}$ ,  $\overline{\sigma\varphi_0} = 2200 \text{ ka}^{-1}$  and  $\mu = 0.6 \text{ mm}^{-1}$  comparable to the average values obtained for the samples  
677 used in this study.

678

679 **Figure 2)** Study area and sampling sites, Southeast Pamir, China. Glacial and landslide boulders were  
680 resampled from three different sites along the Tashkurgan valley. The age ranges represent the  $^{10}\text{Be}$   
681 ages of boulder surfaces previously determined by Seong et al. (2009a) (8–9 ka), Yuan et al. (2013)  
682 (14–15 ka) and Owen et al. (2012) (65–87 ka).

683

684 **Figure 3)** View of the boulders sampled for this study. The red arrows point to the sample locations.

685

686 **Figure 4)** (a) View of Muztagh–2  $^{10}\text{Be}$  sample previously taken by Yuan et al. (2013) in 2010. (b)  
687 View of the same sample as in (a) sampled in 2013 as non-eroding known-age sample for calibration of  
688 luminescence-depth profiles. (c) Variation of the normalized natural sensitivity-corrected IRSL residual  
689 signal ( $L_n/T_n$ ) with depth into i) the bottom of a > 2-cm deep chiseled surface where Muztagh–2  $^{10}\text{Be}$   
690 sample had been collected (red circles), and ii) the natural varnished surface of the boulder (black  
691 circles). Each data point represents the signal measured from at least one whole rock slice coming from  
692 a certain depth into the boulder and thus represents the average luminescence at that depth. The error  
693 bars represent one standard error. For normalization, the  $L_n/T_n$  value of each slice was divided by the  
694 average of saturated  $L_n/T_n$  values measured from depths > 20 mm (i.e. depths in field saturation) in the

695 corresponding profile. The solid lines show the best simultaneous fits to both data sets using Eqn. 4  
696 with the surface bleaching rate  $\overline{\sigma\varphi_0}$  and the light attenuation coefficient  $\mu$  as shared parameters  
697 between the two fits. The fittings were done using Poisson weighting ( $w_i = 1/y_i$ ).

698

699 **Figure 5)** Variation of the normalized natural sensitivity-corrected IRSL signal ( $L_n/T_n$ ) with depth in  
700 all samples. Each data point is an average of the residual signal measured from at least three intact rock  
701 slices of the same depth coming from parallel cores ( $< 5$  cm apart) drilled into the same surface. The  
702 error bars represent one standard error. The normalization factor was obtained by averaging the  $L_n/T_n$   
703 values at depths  $> 20$  mm (i.e. depths in field saturation) for individual profiles. The visually-  
704 indistinguishable overlapping solid lines indicate the best fits of Eqns. 4 and 8 to the data points,  
705 resulting in the apparent luminescence surface-exposure age and erosion rate as model parameters.  $\overline{\sigma\varphi_0}$   
706 was set to  $2165 \text{ ka}^{-1}$  as the shared parameter value between all the fits and  $\mu$  was free to float as the  
707 sample-dependent parameter.  $\dot{D}$  and  $D_o$  had the same values as in Table 1. The fittings were performed  
708 using Poisson weighting ( $w_i = 1/y_i$ ). The dashed and dotted lines represent erosion-free model  
709 profiles obtained by replacing the time in Eqn. 4 with (i) the  $^{10}\text{Be}$  age of the same surface and (ii)  
710 infinity.

711

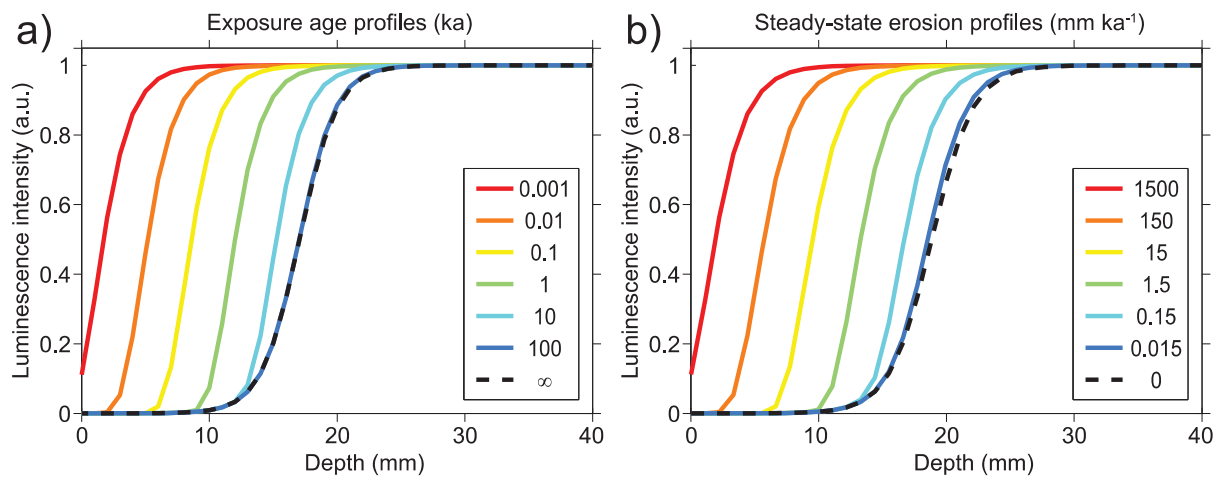
712 **Figure 6)** The model dependence of luminescence-depth profiles on erosion rate and exposure time. (a)  
713 Profiles generated by setting  $t$  in Eqn. 4 to a particular age (from 0.1 a to 100 ka) and then fitting these  
714 modelled profiles with Eqn. (8) using erosion rates of 0 and  $1.5 \text{ mm ka}^{-1}$ . The equilibrium age limit (see  
715 text) is indicated by the extrapolation of the steady-state part of the  $1.5 \text{ mm ka}^{-1}$  curve onto the zero  
716 erosion rate curve. The transition zone between the time ranges in which the profile eroding at  $1.5 \text{ mm}$

717  $ka^{-1}$  acts as chronometer or an erosion-meter is indicated by the points A and B arbitrarily defined to lie  
718 10% within the chronometer and erosion-meter parts of the 1.5-mm  $ka^{-1}$  curve, respectively. (b)  
719 Modelled profiles generated as in (a) but using different erosion rates between 0 and 1500 mm  $ka^{-1}$ ,  
720 showing their respective equilibrium ages on the zero erosion rate curve.

721

## **Table captions**

722 **Table 1)** Summary of samples, model parameter values, luminescence surface-exposure ages and  
723 erosion rates. All the  $^{10}\text{Be}$  ages were calculated using the CRONUS online calculator version 2.3  
724 (Balco et al., 2008) with high latitude/sea level production rate of 4.01 (Borcher et al., 2016), assuming  
725 standard atmosphere, zero erosion and the time-dependent Lal/Stone (2000) spallation scaling scheme,  
726 and are normalized to the “07KNSTD” isotope ratio standardization. The uncertainties include errors  
727 associated with scaling and calibration (external uncertainty).



728 **Figure 1)**

729

730

731

732

733

734

735

736

737

738

739

740

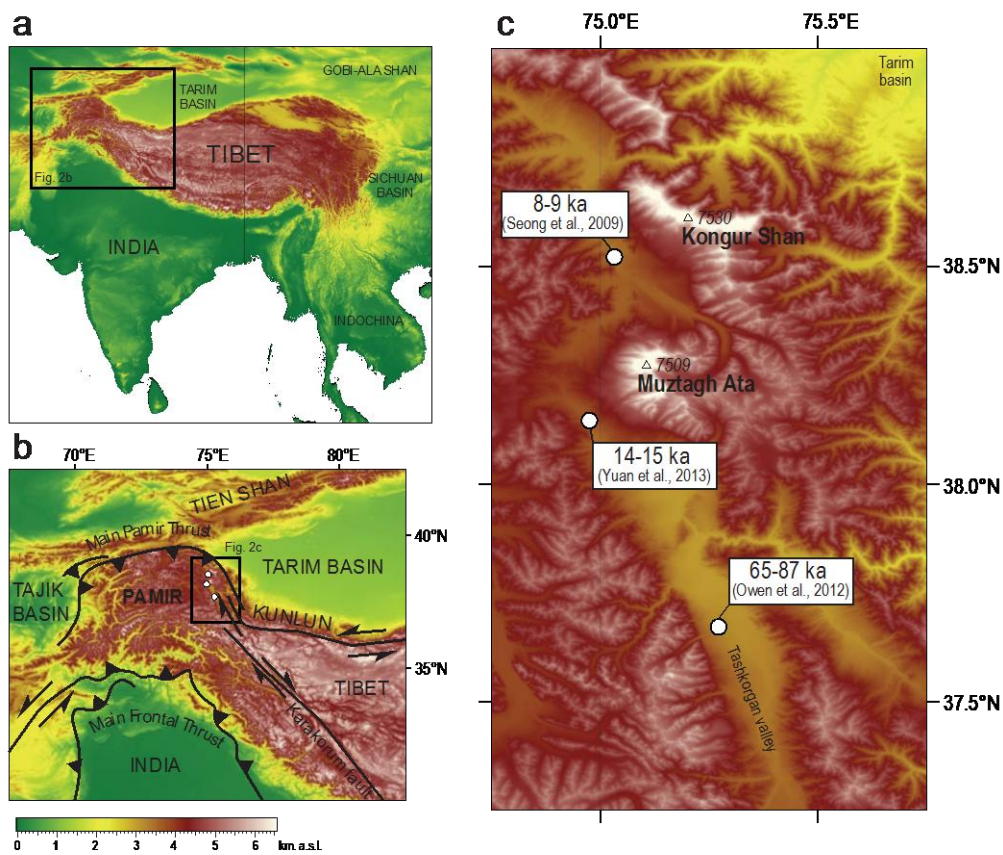


**Figure 2)**



759 **Figure 3)**

a)  $^{10}\text{Be}$  sampling



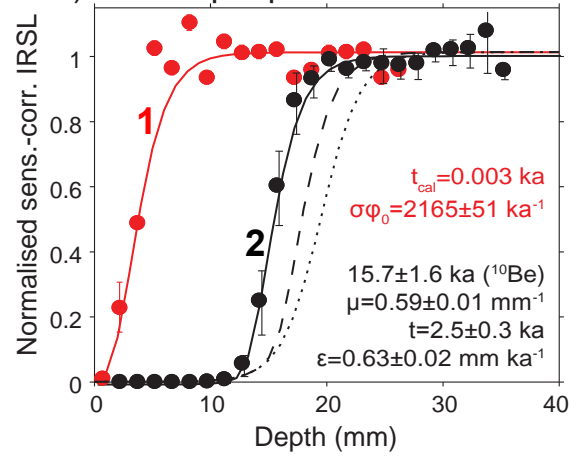
August 2010

b) OSL sampling



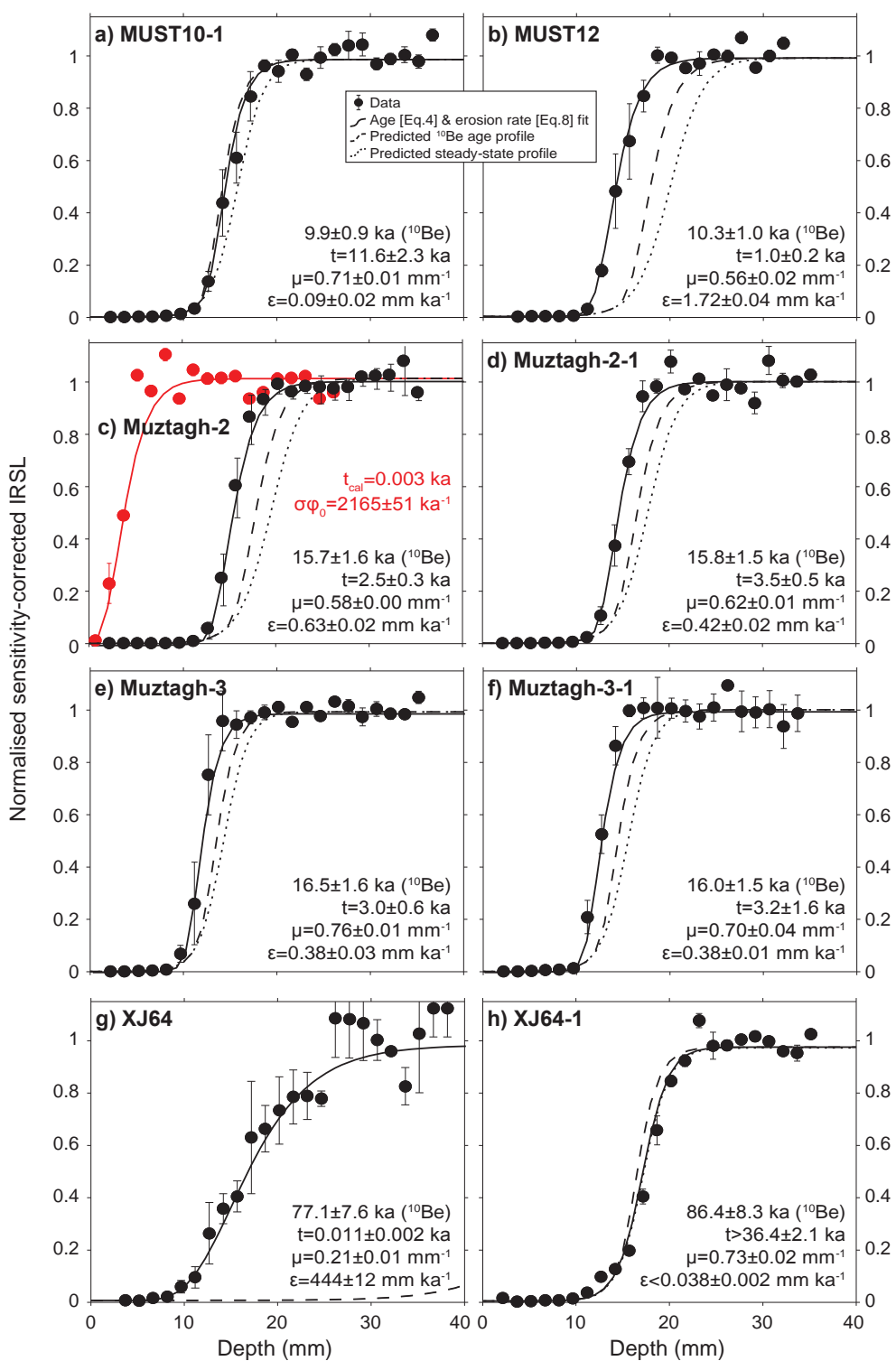
July 2013

c) OSL depth profiles

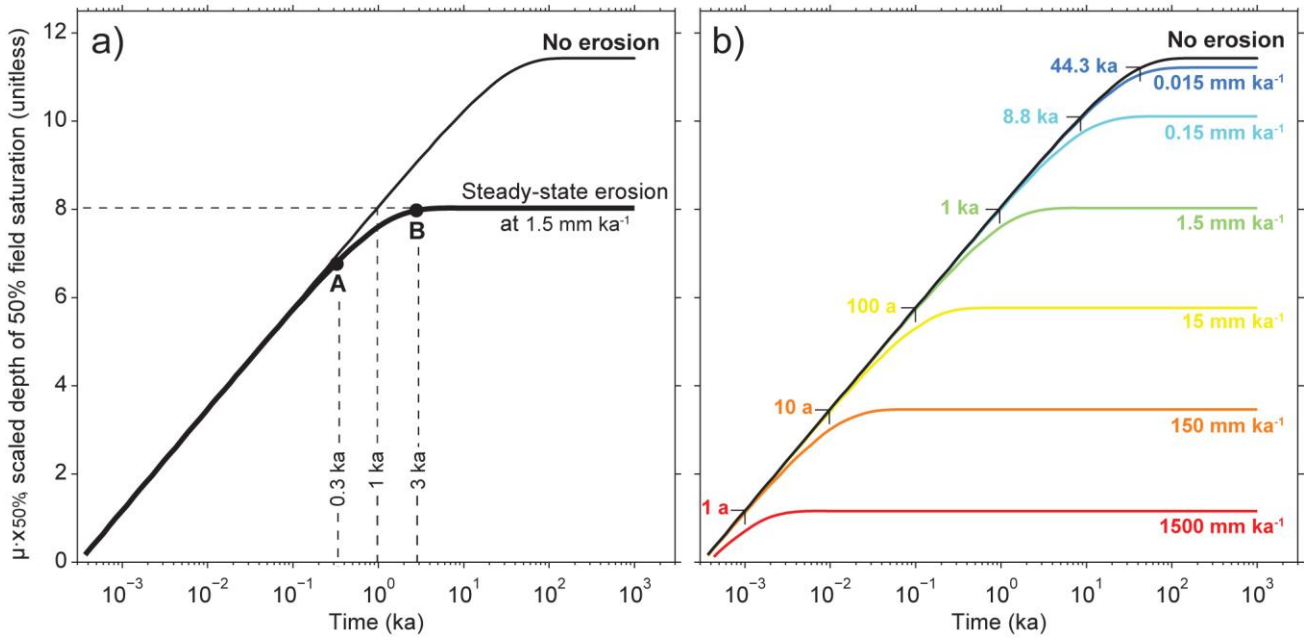


760 **Figure 4)**

761  
762  
763  
764  
765  
766  
767  
768  
769  
770  
771  
772  
773  
774  
775  
776  
777  
778



779 **Figure 5)**



780 **Figure 6)**

Sample name	Landform	Lithology	$\dot{D}$ (Gy ka <sup>-1</sup> ) ± se	$D_0$ (Gy) ± se	Age model		Erosion rate model		Published <sup>10</sup> Be age* ka ± se	<sup>10</sup> Be age Reference
					$\mu$ mm <sup>-1</sup> ± se	age ka ± se	$\mu$ mm <sup>-1</sup> ± se	erosion rate mm ka <sup>-1</sup> ± se		
MUST10-1	Moraine	Granite gneiss	7.99±0.14	276±23	0.71±0.01	11.6±2.3	0.71±0.01	0.09±0.02	9.9±0.9	Liu et al. (in review)
MUST12	Moraine	Granite gneiss	6.98±0.15	264±7	0.56±0.02	1.0±0.2	0.56±0.02	1.72±0.04	10.3±1.0*	Seong et al. (2009a)
MUZTAGH-2	Landslide	Granite gneiss	5.45±0.09	238±34	0.59±0.01	2.5±0.3	0.58±0.00	0.63±0.02	15.7±1.6*	Yuan et al. (2013)
MUZTAGH-2-1	Landslide	Granite gneiss	6.49±0.10	214±16	0.63±0.01	3.5±0.5	0.62±0.01	0.42±0.02	15.8±1.5	Liu et al. (in review)
MUZTAGH-3	Landslide	Granite gneiss	6.19±0.11	176±12	0.77±0.01	3.0±0.6	0.76±0.01	0.38±0.03	16.5±1.6*	Yuan et al. (2013)
MUZTAGH-3-1	Landslide	Granite gneiss	6.23±0.11	225±13	0.73±0.03	3.2±1.6	0.70±0.04	0.38±0.01	16.0±1.5	Liu et al. (in review)
XJ64	Moraine	Granodiorite	7.33±0.15	245±18**	0.21±0.01	0.011±0.002	0.21±0.01	444±12	77.1±7.6*	Owen et al. (2012)
XJ64-1	Moraine	Quartzite	2.72±0.06	320±12	0.73±0.02	>36.4±2.1	0.73±0.02	<0.038±0.002	86.4±8.3	Liu et al. (in review)

782 \* The age was recalculated for consistency with those in Liu et al. (in review).

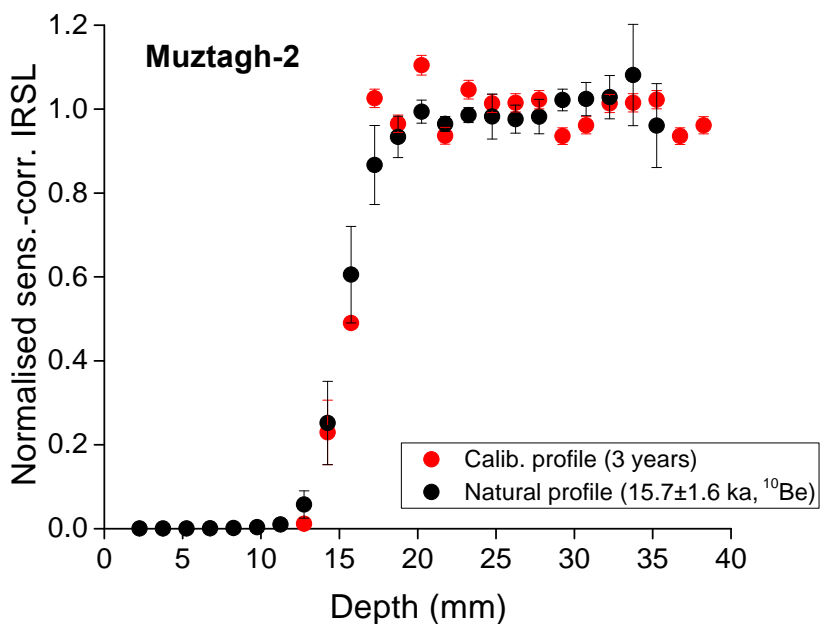
783 \*\* No  $D_0$  was measured for this sample. This is an average of the  $D_0$  values measured for the other samples.

784 **Table 1)**

785 **Supplementary material**

Sample Name	$^{238}\text{U}$ (Bq kg $^{-1}$ ) $\pm$ se	$^{226}\text{Ra}$ (Bq kg $^{-1}$ ) $\pm$ se	$^{232}\text{Th}$ (Bq kg $^{-1}$ ) $\pm$ se	$^{40}\text{K}$ (Bq kg $^{-1}$ ) $\pm$ se	Beta dose rate (Gy ka $^{-1}$ ) $\pm$ se	Gamma dose rate (Gy ka $^{-1}$ ) $\pm$ se	Mean K-feldspar grain size $\mu\text{m}$
MUST10-1	73 $\pm$ 9	109.1 $\pm$ 1.2	146.2 $\pm$ 1.2	1274 $\pm$ 22	3.39 $\pm$ 0.06	3.48 $\pm$ 0.09	800
MUST12	34 $\pm$ 12	31 $\pm$ 1	58.7 $\pm$ 1	1469 $\pm$ 27	2.58 $\pm$ 0.05	2.06 $\pm$ 0.03	1000
MUZTAGH-2	48 $\pm$ 12	34 $\pm$ 1	77.9 $\pm$ 1.2	931 $\pm$ 21	2.68 $\pm$ 0.06	1.89 $\pm$ 0.03	400
MUZTAGH-2-1	27 $\pm$ 8	32 $\pm$ 0.7	97.5 $\pm$ 1.1	1230 $\pm$ 22	3.00 $\pm$ 0.05	2.34 $\pm$ 0.03	600
MUZTAGH-3	65 $\pm$ 11	112.8 $\pm$ 1.4	109.7 $\pm$ 1.3	750 $\pm$ 17	2.99 $\pm$ 0.07	2.66 $\pm$ 0.09	400
MUZTAGH-3-1	45 $\pm$ 9	49 $\pm$ 0.8	91.9 $\pm$ 1.2	1061 $\pm$ 21	2.79 $\pm$ 0.05	2.26 $\pm$ 0.05	600
XJ64	52 $\pm$ 9	66 $\pm$ 1	91.5 $\pm$ 1.2	1229 $\pm$ 24	2.51 $\pm$ 0.04	2.51 $\pm$ 0.06	1000
XJ64-1	24 $\pm$ 7	19.5 $\pm$ 0.6	23.2 $\pm$ 0.7	366 $\pm$ 10	1.19 $\pm$ 0.04	0.70 $\pm$ 0.02	150

786 **Table S1)** Summary of radionuclide concentrations, infinite matrix beta and gamma dose rates and K-feldspar  
 787 grain sizes as used in the calculation of total effective dose rate.



805

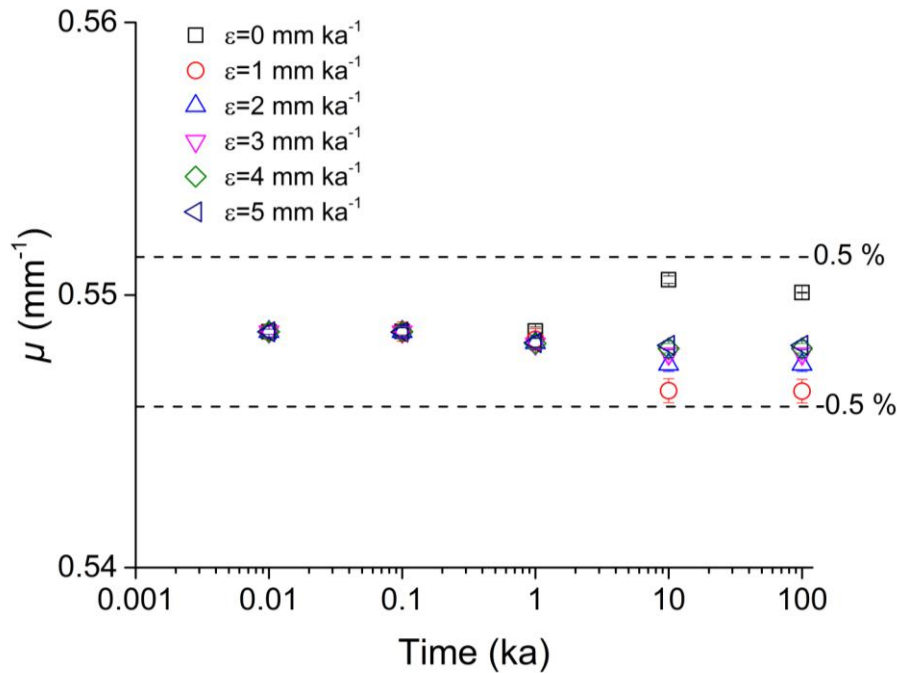
806 **Fig. S1)** The 3-year old calibration profile (profile 1, Fig. 4c) superimposed on the natural profile (profile 2, Fig.  
 807 4c) by adding 12 mm to the depths of profile 1. The two profiles are indistinguishable, confirming that any effect  
 808 of signal instability on the shape of the profile is negligible over a timescale of up to ~16 ka.

810

811 **Sensitivity of the fitted value of  $\mu$  to erosion rate ( $\epsilon$ ) and exposure time ( $t$ )?**

812 In order to investigate the possible effect of erosion on  $\mu$ , we numerically simulated profiles, using  
813 Eqns. (1), (2), (3) and (5), for a range of erosion rates from 0 to 5 mm ka<sup>-1</sup> over a wide range of  
814 exposure times from 1 a to 100 ka. We then fitted the resulting modelled profiles with Eqn. (4) to  
815 determine the best-fit value for  $\mu$  (Fig. S2). The variation in the resulting value of  $\mu$  obtained using the  
816 age model (i.e. no erosion) when fitted to these simulated profiles affected by erosion is < 0.5% around  
817 the true value over an exposure time of up to 100 ka.

818



829 Fig. S2) Dependence of fitted  $\mu$  on apparent age and erosion rate using numerically simulated data.